CrossMark

Triggering Mechanism for Eruption of Two Filaments Observed by the Solar Dynamics Observatory, Nobeyama Radioheliograph, and RHESSI

Sujin Kim[1] and Vasyl Yurchyshyn[2]

[1] Korea Astronomy and Space Science Institute, Daejeon,305-348, Republic of Korea
[2] Big Bear Solar Observatory, New Jersey Institute of Technology, 40386 North Shore Lane, Big Bear City, CA 92314, USA

Abstract

We investigate the eruptive process of two filaments, which is associated with an M-class flare that occurred in 2011 August 4. The filaments are partly overlapped, one in the active region and the other just beside it, and erupt together as a halo coronal mass ejection. For this study, we used the Atmospheric Imaging Assembly and the Heliospheric Magnetic Imager on board the Solar Dynamics Observatory, the Nobeyama Radioheliograph 17 GHz, and the RHESSI Hard X-ray satellite. We found three distinct phases in the microwave flux profile and in the rising pattern of the filaments during the event. In the first phase, there was weak nonthermal emission at 17 GHz and hard X-rays. Those nonthermal sources appeared on one edge of the western filament (F2) in the active region. The F2 began to be bright and rose upward rapidly, while the eastern filament (F1), which was extended to the quiet region, started to brighten from the peak time of the 17 GHz flux. In the second phase, the nonthermal emission weakened and the F2 rose up slowly, while the F1 began to rise up. In the third phase, two filaments erupted together. Since the F1 was stable for a long time in the quiet region, breaking the equilibrium state of the F1 would be decisive for the successful eruption of two filaments and it seems clear that the evolution of the F2 provoked the unstable F1. We suggest that tether-cutting reconnection between two overlapped filaments triggers the eruption of the two filaments as a tangled identity.

Unified Astronomy Thesaurus concepts: Solar flares (1496); Solar filaments (1495); Solar corona (1483); Solar filament eruptions (1981)

1. Introduction

Filament eruptions associated with solar flares may develop into high-speed coronal mass ejections (CMEs), which often disturb the near-Earth space environment and cause strong geomagnetic storms. Filaments are cool and dense chromospheric plasma supported by magnetic fields above the photospheric polarity inversion line. It is thought that the associated magnetic fields are carrying a strong electric current and are either highly sheared or have a helical structure comprising a filament channel. A quasi-equilibrium state of a filament channel is maintained when the downward magnetic tension is balanced by the upward magnetic pressure (e.g., Cowling 1957). However, the quasi-equilibrium can be often disrupted by an internal or external cause, which may lead to an eruption when magnetic fields and plasma are expelled from the solar coronal into interplanetary space.

There are several mechanisms that may trigger a filament eruption. Moore et al. (2001) suggested that a tether-cutting reconnection in a sheared core field may remove fields lines that tie twisted or sheared fields to the photosphere thus allowing the core fields to rapidly expand upward. On the other hand, Antiochos (1998) proposed a breakout model where external tether-cutting reconnection reduces the magnetic flux above the filament system thus allowing the eruption to be initiated. Various magnetohydrodynamic (MHD) instabilities were also considered as a trigger of eruptions. Thus, the kink instability may arise in a twisted magnetic flux tube leading to

destabilization of a magnetic structure (Török & Kliem 2004). A strong vertical gradient in overlying magnetic fields, which can be described using a decay index, is thought to be favorable for the development of torus instability (Kliem & Török 2006). These and other trigger mechanisms have been extensively studied in the past (e.g., Török & Kliem 2005; Kumar et al. 2012; Vemareddy et al. 2017; Wang et al. 2017; Jing et al. 2018; Woods et al. 2018; Kang et al. 2019; Zou et al. 2019). Ishiguro & Kusano (2017) proposed a new type of instability, which they called a double-arc instability (DAI). These authors modeled a sigmoidal configuration by a double-arc electric current system and found that it can be destabilized without the weakening of the overlying magnetic fields, which is usually required for initiating a torus instability. Later, Kusano et al. (2020) presented a flare prediction model based on a "trigger-reconnection" approach that exploits the DAI. Although it is still debatable as to which mechanism is responsible for triggering eruptions (e.g., Aulanier et al. 2009; Savcheva et al. 2012; Patsourakos et al. 2020), it seems that different mechanisms may be realized in the solar atmosphere depending on the existing physical conditions and/or the magnetic configuration, while each mechanism could be closely linked to or provides the condition to be taken place, and finally complete an eruption.

In this paper, we focus on an eruption of two distinct but spatially overlapped filaments situated within different magnetic field environments (active and quiet regions). In Section 2 we describe multiwavelength data we used with emphasis on the ascending motion of the filaments and in the next Section we present the results and discussion.
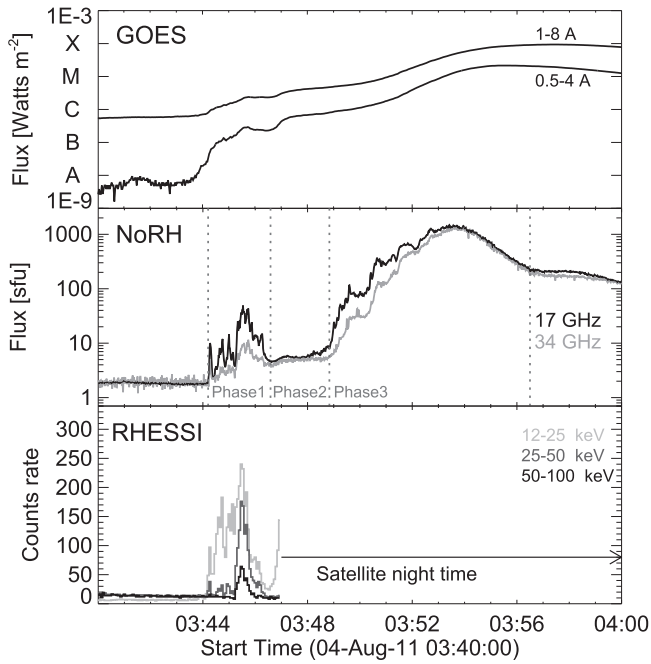
Figure 1. M9.3 flare flux time profiles from top to bottom: GOES low 1–8 Å and high 0.5–4 Å energy bands, microwave NoRH 17 GHz (black line) and 34 GHz (gray line) flux, and RHESSI X-ray counts rate in 12–25 keV, 25–50 keV, and 50–100 keV bands. The vertical dotted lines in the middle panel mark the flare phases.

2. Observations

We investigated an eruption of two filaments associated with a GOES M9.3 X-ray class solar flare (SOL2011-08-04T03:41) that occurred in NOAA active region (AR) 1261 on 2011 August 4. For the study, we used 304 Å and 94 Å EUV data obtained by the Atmospheric Imaging Assembly (AIA; Lemen et al. 2012) on board the Solar Dynamics Observatory (SDO;

Pesnell et al. 2012) as well as 17 GHz data acquired with the Nobeyama Radioheliograph (NoRH; Nakajima et al. 1985; Takano et al. 1997). The microwave data have a spatial resolution of 10″ and a time cadence of 1 s. The AIA data have a spatial resolution of 1″.2 and a 12 s time cadence. In addition, we used longitudinal magnetograms from the Helioseismic and Magnetic Imager (HMI; Scherrer et al. 2012) on board SDO and hard X-ray data from the RHESSI satellite (Lin et al. 2002).

Figure 1 shows X-ray (top), microwave (middle), and hard X-rays (bottom) intensity time profiles. The X-ray flare started at 03:41 UT and peaked at 03:57 UT after which the X-ray flux was gradually decreasing over a period of several hours. The NoRH microwave flux profile shown in Figure 1 reveals that there were three distinct flare phases. During Phase 1, the microwave flux began to increase at 03:44:12 UT, peaked at around 03:45:30 UT, and flattened out at around 03:46:35 UT. Phase 1 was also associated with strong hard X-ray emission with energies up to 100 keV; however, there are no hard X-ray (HXR) measurements after Phase 1 due to the RHESSI satellite entering the night-side of the Earth. In Phase 2 (03:46:35-03:49:35 UT), the microwave flux remained nearly stable but elevated above the quiet Sun level without noticeable spikes, while Phase 3 (03:49-03:56:30 UT) includes the major flare stage with the peak 17 GHz flux of 1450 sfu starting at 03:48:50 UT.

Figure 2 shows the evolution of the filaments as captured in AIA 94 Å and 304 Å EUV channels. The AIA 304 Å channel images He II emission originating in the chromosphere and the transition region with a characteristic temperature of log $T = 4.7$ and the AIA 94 Å channel images Fe XVIII emission formed at 7 MK in hot flare plasmas (Lemen et al. 2012). Two dark curved filaments, F1 and F2, can be seen inside the white box prior the flare onset (Figure 2(a)). They appear to overlap with each other at their endpoints thus forming a configuration
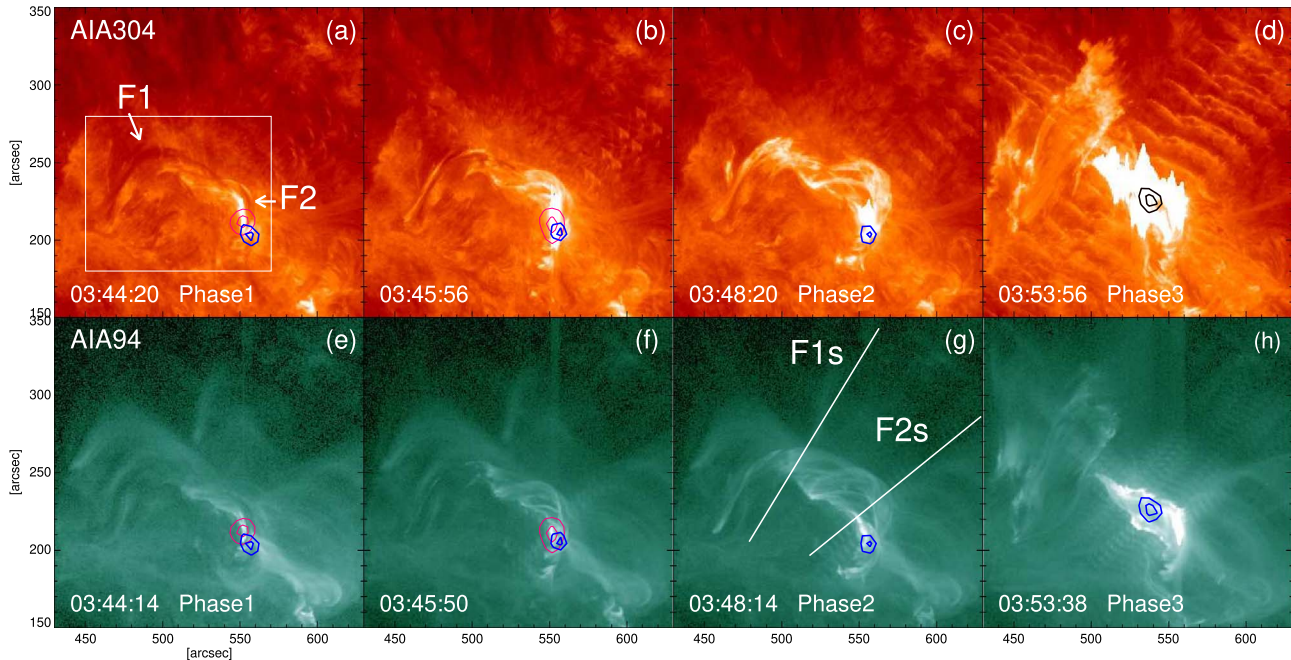

Figure 2. Time sequence of AIA 304 Å (top) and 94 Å (bottom) images. Panels (a) and (e) show the onset of Phase 1, panels (b) and (f) capture the peak of Phase 1, while panels (c), (g), and (d), (h) represent Phase 2 and Phase 3, respectively. The blue and red contours are NoRH 17 GHz and RHESSI 20–40 keV measurements, respectively. The contour levels are plotted at 70% and 90% of their maximum intensity. The line segments in panel (g) indicate directions of the eruption of filaments F1 and F2 and they also represent slits used to produce time-space plots shown in Figure 3. A color version of this figure is available in the online journal.
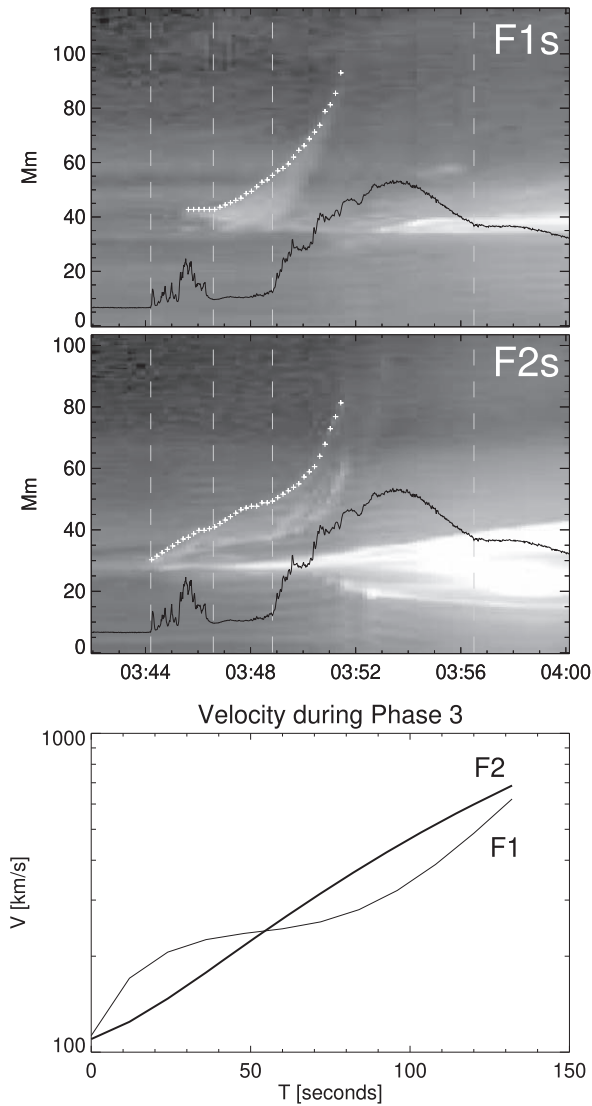
Figure 3. Upper and middle panels: time-space plots made along the slits shown in Figure 2(g). The y-axis is along the direction of the eruption and the leading edge of the eruptions is marked with white cross symbols. The vertical dotted lines separate periods of nonthermal emission, as well as Phase 1, Phase 2, and Phase 3 of the flare. In both panels the solid curve represents NoRH 17 GHz emission. Bottom panel: velocity profiles during Phase 3 for F1 (thin) and F2 (thick solid line).

reminiscent of a double-arc system (Ishiguro & Kusano 2017). During Phase 1, a compact nonthermal source was observed in microwave and HXR spectral ranges at the southern end of the F2 (Figures 2(a) and (e)), after which the F2 brightened and expanded upward. Subsequently, filament F1 only partly brightened (see Figures 2(b) and (f)). The two filaments appear to be independent magnetic structures, and since there were no nonthermal sources associated with the F1, we may speculate that the expanding filament F2 may have directly affected the F1 thus resulting in the brightening of a part of the F1. In Phase 2, both F1 and F2 expanded upward as a single entity (2(g)) and then erupted together in Phase 3 (panels (d) and (h) in 2). A posteruption arcade (PEA) with a bright footpoint area formed at the location of the F2 (2(h)), while the nonthermal microwave source shifted in the northeast direction and became cospatial with the central part of the PEA (Figures 2(d) and (h)).

In order to examine the upward motion of F1 and F2 in detail, we made a time-space plot (Figure 3) using two slits, F1s and F2s, which were aligned with the filament expansion path (See Figure 2(g)). As it follows from the plots, during Phase 1, the F2 brightened and began to rise, while the F1 remained stationary and undisturbed to only brighten near the peak time of the 17 GHz flux. Considering that the F1 brightened at a location near the expanding filament F2, it is likely that the ascending F2 initiated interaction with F1 at the peak time of Phase 1 and the brightness increase may be due to reconnection between magnetic structures of F1 and F2. In Phase 2, the leading edge of the joint F1 and F2 system continued to expand upward, after which the system accelerated and disappeared from the AIA field of view (FOV) before the microwave emission peak time in Phase 3. We have estimated the speed and acceleration of each erupting filament by tracing the bright leading edge (white crosses in Figure 3). The rising speed of the F2 was estimated to be around $160 \, \mathrm{km \, s^{-1}}$ during the early stage of Phase 1 and Phase 2, and it accelerated up to $330 \, \mathrm{km \, s^{-1}}$ during Phase 3. Meantime, the rising speed of the F1 was estimated at $95 \, \mathrm{km \, s^{-1}}$ during Phase 2, and then increased up to $670 \, \mathrm{km \, s^{-1}}$ during Phase 3, which is twice as fast as that of the F2. Plots of the logarithm of the velocity profiles during Phase 3 (bottom panel in Figure 3) show that the F1 exhibits a well-defined linear range between $t = 30 \, \mathrm{s}$ and $t = 100 \, \mathrm{s}$, indicating an exponential growth, while the F1 profile shows a shorter linear range during the late stage of the eruption. It partially may be due to the fact that the F1 slit was positioned further away from the apex of the erupting structure; thus, the velocity of the F1 side branch may not have the same dynamics as the apex of the erupting structure. The linear growth in the logarithm of velocity plots indicates that these eruptions were likely to be driven by an MHD instability (Ishiguro & Kusano 2017).

Figure 4 shows photospheric longitudinal magnetic fields obtained by the HMI instrument with overplotted outlines of filaments F1 and F2 (red), and the microwave source (blue). Filament F2 was situated above the polarity inversion line enclosing the main sunspot on the west, while one endpoint of F1 was anchored at the main sunspot area and the other endpoint was rooted in a quiet Sun area. The high-energy sources situated at the southern leg of F2 initially appeared on the polarity inversion line. The comparison of the magnetic flux in this area (white box in the two right panels in Figure 4) measured before and after the eruption, revealed that both positive and negative magnetic flux decreased at locations indicated by the white (positive flux) and black (negative flux) arrows in Figure 4. This cancellation of the photospheric magnetic field indicates a magnetic reconnection event in the lower atmosphere (Van Ballegooijen & Martens 1989), which could be a trigger of the nonthermal process that occurred at F2 during Phase 1.

3. Result and Discussion

We studied a joint eruption of two filaments located in the core of an AR and in its vicinity. The filaments were observed partially overlapping and erupted as one entity. The eruption induced a strong M-class flare and further developed into a halo CME. We examined the evolution of the eruption process using flux profiles and imaging data obtained in the EUV and microwave range, as well as magnetic field measurements in
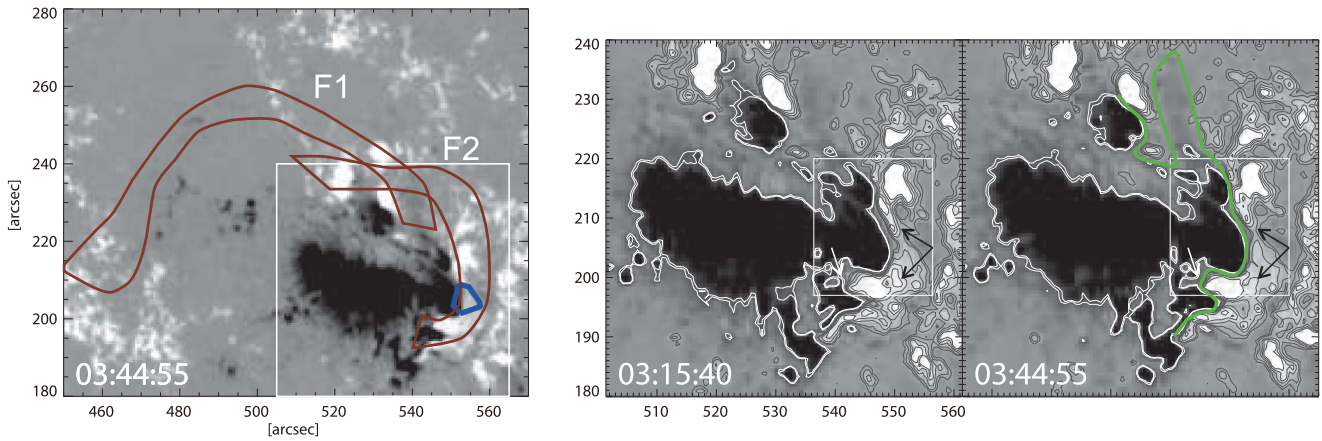
Figure 4. Left panel: background is an HMI magnetogram with outlines of filaments F1 (left) and F2 (right) and contours of the microwave source plotted at the 90% level of the maximum intensity (blue). The FOV is the same as that outlined by the white box in Figure 3(a). Right panel: HMI magnetograms acquired about 30 minutes before the event (left) and during Phase 1 (right). Black contours outline positive magnetic fields of 50, 100, 200, 300, and 400 G and white contours outline negative magnetic field of −250 and −300 G. Arrows in the white box indicate regions where the magnetic flux decreased and a green solid curve is a polarity inversion line.
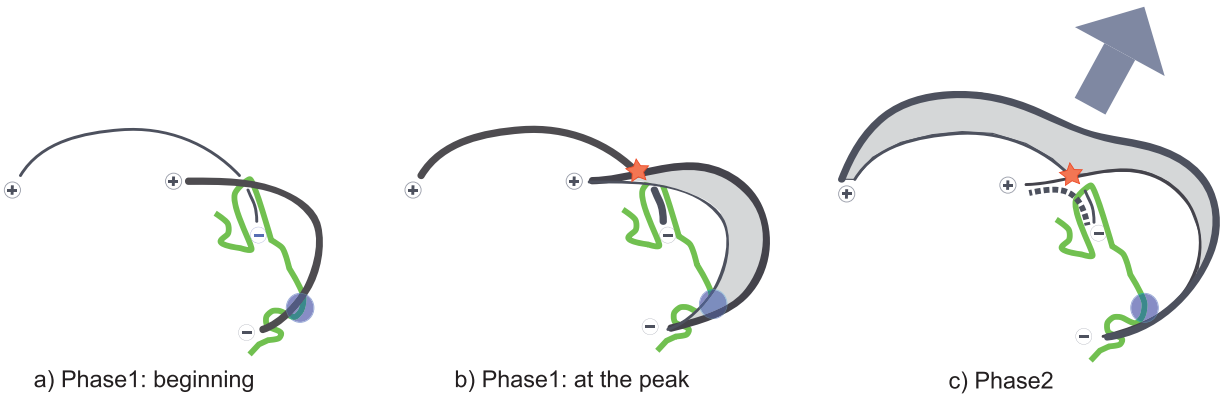

Figure 5. Possible scenario of the eruption of the two filaments. Solid lines represent the filaments and their magnetic connectivity. The green line is the polarity inversion line (see Figure 4) and the blue circle marks the position of the microwave source.

order to reveal a crucial trigger of the filament eruption and the flare.

Our scenario suggests that a two-step reconnection process occurred before the eruption of F1 and F2 filaments. Yurchyshyn et al. (2015) reported that a slow rise flare with multistep reconnection process may indicate the formation of an eruptive flux rope. The flux profile of the NoRH 17 GHz showed three distinct phases, and the patterns of ascending motion of the two filaments are quite relevant to each phase. Based on the results, we speculate that the event evolved as depicted in Figure 5. In Phase 1, the first reconnection event took place at the southern leg of F2 where the microwave source appeared.

HMI data showed that there was a magnetic flux cancellation event near the polarity inversion line where the first reconnection occurred in Phase 1. It implies that the magnetic reconnection took place in the low atmosphere and a new flux may have been added to F2, which caused F2 to become unstable. Thus, the magnetic flux cancellation could have triggered the studied event.

Heating and injection of magnetic flux caused by reconnection destabilized F2, which began to expand and rise. Continuous expansion of F2 led it to encounter F1, causing F1 to brighten due to the second reconnection event between F1 and F2 at the peak time of Phase 1. The occurrence of the second reconnection is evidenced by the enhanced brightness

of F1 in EUV images. As a result, F1 and F2 joined and created a large-scale unstable magnetic structure that slowly expanded upward during Phase 2 (Figure 5(c)). Finally, in Phase 3, the F1–F2 system rapidly accelerated and gave rise to a solar flare with a nonthermal source near the top of the PEA in accordance with the standard flare model (Shibata 1998). We advocate that the second reconnection created a double-arc type magnetic structure with enhanced currents, which may may have triggered the onset of DAI.

Prior to the flare, there was a magnetic flux cancellation event near the polarity inversion line where the first reconnection occurred in Phase 1. It implies that the magnetic reconnection took place in the low atmosphere and hence a new flux rope may have formed there (Van Ballegooijen & Martens 1989). This new flux rope probably interacted with F2 above and transferred magnetic flux and energy to the entire structure of F2. Thus, the magnetic flux cancellation could have triggered the studied event. However, this flux rope itself was not enough to disturb and trigger the eruption of the F1, and it maybe owes to the overlying F1 subpress one arm of the F2.

On the other hand, using 3D MHD simulations Kusano et al. (2012) demonstrated that the type of the small-scale magnetic field emerging near the polarity inversion line may affect the possibility of the eruption onset. Authors categorized the small-scale magnetic field into four types based on the shear of the

magnetic field relative to the large-scale major field, and found that two of the configurations (opposite polarity (OP) and reversed shear (RS)) favor triggering a solar eruption. Interestingly, the magnetic environment in our event contains a small-scale RS system (immediately southeast of the microwave source), which is similar to the RS+ configuration depicted in Figure 5 of Kusano et al. (2012). This implies that the preflare magnetic configuration found in the studied event was favorable for developing an instability and triggering an eruption.

The onset of a filament eruption was studied starting from the very early stage that includes flux emergence and cancellation up to the last stage such as the development of torus instability. Based on our investigation, we suggest that the DAI is a viable candidate for triggering the eruption of two closely positioned and partially overlapping filaments. Indeed, Ishiguro & Kusano (2017) modeled a double arc (DA) structure based on a sigmoidal magnetic field configuration often observed in ARs. The tether-cutting reconnection is essential to construct DA loops and hence induce the DAI. Recently, there were studies that presented the process of the eruption based on the observations and NLFFF simulation for AR sigmoidal structure, and suggested the DAI would be an intermediate trigger for the eruption before the torus instability (Woods et al. 2018; Kang et al. 2019). Woods et al. (2018) investigated two separate flux ropes and found, interestingly, that one flux rope erupted while the other did not even with a higher twist. They proposed that the tether-cutting reconnection of the flux rope lead to the onset of DAI. Our event consists of two distinct filaments with DA magnetic configuration as a base, which is similar to but not the typical sigmoid that has been referred to previously (Ishiguro & Kusano 2017; Woods et al. 2018; Kang et al. 2019; Kusano et al. 2020). The event shows interaction between filaments, which implies tether-cutting reconnection may lead the effective instability for filaments to destabilize and erupt. And also, it seems clear that the activity inducing the interaction between filaments, the first reconnection in the Phase 1, is an essential part of the eruptive process. Our event suggests that the first reconnection before the eruption initiates the tether-cutting reconnection in filament systems with DA magnetic configuration, and the tether-cutting reconnection and resulting DAI play a key role to accelerate the eruptive process.

ORCID iDs

Sujin Kim ⓘ https://orcid.org/0000-0002-5004-7734
Vasyl Yurchyshyn ⓘ https://orcid.org/0000-0001-9982-2175

References

Antiochos, S. K. 1998, ApJ, 502, L181
Aulanier, G., Török, T., Démoulin, P., & DeLuca, E. E. 2009, ApJ, 708, 314
Cowling, T. G. 1957, Magnetohydrodynamics (New York: Interscience), 552
Ishiguro, N., & Kusano, K. 2017, ApJ, 843, 101
Jing, J., Liu, C., Lee, J., et al. 2018, ApJ, 864, 138
Kang, J., Inoue, S., Kusano, K., Park, S.-H., & Moon, Y.-J. , 2019, ApJ, 887, 263
Kliem, B., & Török, T. 2006, PhRvL, 96, 255002
Kumar, P., Cho, K.-S., Bong, S.-C., Park, S.-H., & Kim, Y.-H. 2012, ApJ, 746, 67
Kusano, K., Bamba, Y., Yamamoto, T. T., et al. 2012, ApJ, 760, 31
Kusano, K., Iju, T., Bamba, Y., & Inoue, S. 2020, Sci, 369, 587
Lemen, J. R., Title, A. M., Akin, D. J., et al. 2012, SoPh, 275, 17
Lin, R. P., Dennis, B. R., Hurford, G. J., et al. 2002, SoPh, 210, 3
Moore, R. L., Sterling, A. C., Hudson, H. S., & Lemen, J. R. 2001, ApJ, 552, 833
Nakajima, H., Sekiguchi, H., Sawa, M., Kai, K., & Kawashima, S. 1985, PASJ, 37, 163
Patsourakos, S., Vourlidas, A., Török, T., et al. 2020, SSRv, 216, 131
Pesnell, W. D., Thompson, B. J., & Chamberlin, P. C. , 2012, SoPh, 275, 3
Savcheva, A., Pariat, E., van Ballegooijen, A., Aulanier, G., & DeLuca, E. 2012, ApJ, 750, 15
Scherrer, P. H., Schou, J., Bush, R. I., et al. 2012, SoPh, 275, 207
Shibata, K. 1998, in Astrophysics and Space Science Library book series, Observational Plasma Astrophysics, Five Years of Yohkoh and Beyond, ed. T. Watanabe, T. Kosugi, & A. C. Sterling (Berlin: Springer), 187
Takano, T., Nakajima, H., Enome, S., et al. 1997, in Coronal Physics from Radio and Space Observations, Proc. of the CESRA Workshop, ed. G. Trottet (Berlin: Springer), 183
Török, T., & Kliem, B. 2004, A&A, 406, 1043
Török, T., & Kliem, B. 2005, ApJL, 630, L97
Van Ballegooijen, A. A., & Martens, P. C. 1989, ApJ, 343, 971
Vemareddy, P., Gopalswamy, N., & Ravindra, B. 2017, ApJ, 850, 38
Wang, D., Liu, R., Wang, Y., et al. 2017, ApJL, 843, L9
Woods, M. M., Inoue, S., Harra, L. K., et al. 2018, ApJ, 860, 163
Yurchyshyn, V., Kumar, P., Cho, K.-S., et al. 2015, ApJ, 812, 172
Zou, P., Jiang, C., Wei, F., Zuo, P., & Wnag, Y. 2019, ApJ, 884, 157